metrology

MDPI

Article

A Two-Dimensional K-Shell X-ray Fluorescence (2D-KXRF) Model for Soft Tissue Attenuation Corrections of Strontium Measurements in a Cortical Lamb Bone Sample

Mihai R. Gherase

Department of Physics, College of Science and Mathematics, California State University, Fresno, CA 93740, USA; mgherase@csufresno.edu

Abstract: Human bones store elements such as calcium, phosphorus, and strontium, and accumulate toxic elements such as lead. In vivo measurements of elemental bone concentration can be done using X-ray fluorescence (XRF) techniques. Monte Carlo (MC) simulations of X-ray interactions were predominantly employed in this field to develop calibration methods that linked XRF measurements to concentrations. A simple and fast two-dimensional K-shell X-ray fluorescence model was developed to compute the KXRF signal of elements in bone and overlying soft tissue samples. The model is an alternative to MC methods and can guide future bone XRF studies. Contours of bone and soft tissue cross sections were elliptical and only KXRF signals from absorption of primary photons were considered. Predictions of the model were compared to Sr KXRF measurements using the bare lamb bone (LB) and the LB with overlying leather. XRF experiments used a small X-ray beam, silicon X-ray detector, and three positioning stages. Linear attenuation coefficients of the leather and LB were measured and used in the model. Measured and model-derived values of the Sr X-rays leather attenuation and Sr Kβ/Kα ratio agreed, but estimated bone Sr concentrations were likely overestimated. Results, approximations, future work directions, and applications were discussed.

Keywords: X-ray fluorescence; calibration; bone; strontium

Citation: Gherase, M.R. A Two-Dimensional K-Shell X-ray Fluorescence (2D-KXRF) Model for Soft Tissue Attenuation Corrections of Strontium Measurements in a Cortical Lamb Bone Sample. *Metrology* **2023**, *3*, 325–346. https://doi.org/10.3390/metrology3040020

Academic Editor: Han Haitjema

Received: 21 July 2023
Revised: 6 September 2023
Accepted: 12 September 2023
Published: 6 October 2023

1. Introduction

In vivo and in vitro X-ray fluorescence (XRF) studies focused on detection, spatial distribution, and concentration measurements of chemical elements in biological tissues date back to more than half a century [1–3]. XRF methods identify elements based on the detection of characteristic X-rays: photons of well-defined energy emitted by atomic electron transitions from upper to lower subshells. In XRF, electron transitions are triggered by core vacancies in K or L atomic subshells produced by photoelectric absorption of incident X-rays. Characteristic hard X-ray photon energies (>1 keV) and their relative emission intensities uniquely identify elements starting with sodium (Na) which emits characteristic X-ray photon energies slightly above 1 keV [4].

XRF is both a sensitive and a nondestructive analytical method, capable of simultaneous detection and quantification of multiple elements in concentrations as low as a few micrograms per gram (μg g^{-1}). Chemical elements found in low concentrations are typically referred to as trace elements. Trace elements play essential roles in the physiology of the human body and of other organisms. It is estimated that a quarter or more of proteins have a metallic trace element in their molecular structure [5–7]. In vivo XRF measurements date back to the 1965 thyroidal iodine study of Hoffer et al. [8]. Past and recent in vivo XRF studies used radioactive sources for atomic excitation such as ^{57}Co [9], ^{109}Cd [10–12], ^{125}I [13,14], or ^{241}Am [15,16]. In the foreseeable future, however, portable and lab-based XRF systems, based on X-ray tubes, are, arguably, the preferable option as they eliminate the safety concerns associated with radioactive sources. Diagnostic, therapeutic, or monitoring purposes of medical or biological XRF studies require placement of absolute or

relative elemental concentration measurements inside or outside a given concentration range. Therefore, medical XRF applications are strongly linked to the accuracy of the calibration method setting the relationship between measurements and the corresponding elemental concentrations.

A reliable calibration method was established for biological XRF measurements of trace elements in the human cortical bone such as lead (Pb) [10], strontium (Sr) [14], barium (Ba), iodine (I), lanthanum (La), and gadolinium (Gd) [15,16] using radioactive sources. The method, abbreviated herein as the coherent calibration method, relied on the spectrometric measurement of the ratio between the XRF and coherent scatter peak. As demonstrated in these studies and others, it was shown that the ratio was proportional with the bone elemental concentration, but it was independent from varying experimental conditions such as bone size and bone and soft tissue attenuation of incident gamma-rays and emergent characteristic X-rays. Unfortunately, a simple extension of the coherent calibration method to XRF applications using X-ray tubes is not feasible as coherently and incoherently (Compton) scattered photons cannot be separated from the continuous observed scattered bremsstrahlung peak by employing spectrometric methods alone. However, one can compute XRF signal from a given photon energy spectrum provided knowledge of several elements: (i) sample shape and excitation-detection geometry, (ii) X-ray attenuation properties of the sample, and (iii) spatial distribution of elements.

Early modelling efforts by Sherman [17] employed atomic cross section knowledge and elemental composition of the sample to compute the XRF intensity (i.e., photon rate, photon fluence, or fluence rate) emitted in the solid angle determined by the X-ray detector area relative to the incident photon irradiation. Initial approximations were: parallel incident and emergent X-rays, homogeneous sample composition and elemental distributions. Applications and subsequent modifications of Sherman equations were later known as the fundamental parameter method (FPM). Its name refers to the atomic parameters describing the physical processes leading to the observed XRF signal: cross sections of the X-ray interactions, probabilities of K and L shells vacancies, fluorescence yields, and emission rates. Initial FPM formulations did not include XRF contributions from coherently and incoherently scattered photons or from electron excitations. Later refinements of the FPM included: secondary XRF [18], scattered photons [19–22], mathematical and computational treatments [23–25], non-parallel X-rays [26], and treatment of XRF observed in a transmitting geometry [27]. FPM was successfully applied to thickness measurements of layers and coatings [28–30], elemental composition of metallic alloys and multilayered samples [31,32], and treatment of depth-dependent elemental distributions [33].

In parallel with FPM developments, Monte Carlo (MC) [34–50] and Boltzmann transport equation [51–55] methods were developed to model X-ray interactions and electron transport more accurately. A detailed description of the evolution, physical processes, and numerical implementations and algorithms is beyond the scope of this paper. Reviews of MC methods in the context of medical physics applications with historical and personal perspectives are published [56–58]. It is important to mention, however, that MC research in radiation physics evolved from early curiosity-driven inquiries to current application-driven frameworks, the current landscape being a blend of general-purpose MC codes that include comprehensive detailed modelling of particle interactions and computationally-efficient models.

In this larger context of modelling approaches to X-ray interactions, the two-dimensional K-shell XRF (2D-KXRF) model described in this paper is in the FPM class: only the relative detected XRF signal from primary absorption interactions of incident photons was computed. The model was initiated by the author's effort to explain the ratios between Sr Kα and Sr Kβ peak areas measured from a bare lamb bone sample and those measured from the bone with an overlying 2.8-mm-thick leather. Demonstrated agreement between model's predictions and experimental results indicates that user-built computationally-efficient XRF models are viable alternatives to general-purpose and specialized MC frameworks.

2. Materials and Methods

2.1. KXRF Lamb Bone Sr Measurements

2.1.1. Experimental Setup

The experimental equipment was presented in our previous publications [59–61]. For clarity, the main experimental equipment is described in this section. The microbeam XRF equipment consisted of: (i) an integrated X-ray tube and polycapillary X-ray lens (PXL) (Polycapillary X-beam Powerflux model, X-ray Optical Systems, East Greenbush, NY, USA), (ii) silicon-drift X-ray detector with integrated pulse-height analyzer (X-123 SDD model, Amptek Inc., Bedford, MA, USA), (iii) XY modular motorized linear positioning stage unit (Newport Co., Irvine, CA, USA).

Schematics of the experimental setup and X-ray detector are provided in Figure 1. The continuous emission X-ray tube was air-cooled, and its target was made of tungsten (W). The built-in PXL was 100 mm in length and 10 mm outer diameter. The X-ray tube voltage and current could be varied in 0.1 kV and 1 μA increments, respectively. During all experiments, the voltage was 50 kV, and the current was 1 mA. X-ray tube and PXL unit was also equipped with a filter wheel placed in front of the PXL. For XRF experiments, a 1.8 mm Al filter was used to reduce the negative effect of the W L-shell characteristic X-rays. Their maximum values of 50 kV and 1 mA were used during the XRF measurements. The circular active area of the detector is 25 mm^2 (or 5.6 mm diameter) and 500 μm thickness and the window consisted of a 12.5 μm-thick beryllium (Be) sheet. The counting rate capability of the detector provided by the manufacturer was 10^5 counts s^{-1}. The manufacturer also provided that the detector's energy resolution measured as Full Width at Half Maximum (FWHM) at 5.9 keV energy and 11.2 μs peaking time is in the 125 eV to 140 eV range. A 20 mm-long aluminum (Al) collimator was attached to the end of the X-ray detector to reduce X-ray scatter. The X-ray detector was mounted on a horizontal Al plate which was attached to the XY modular motorized linear positioning stage unit.

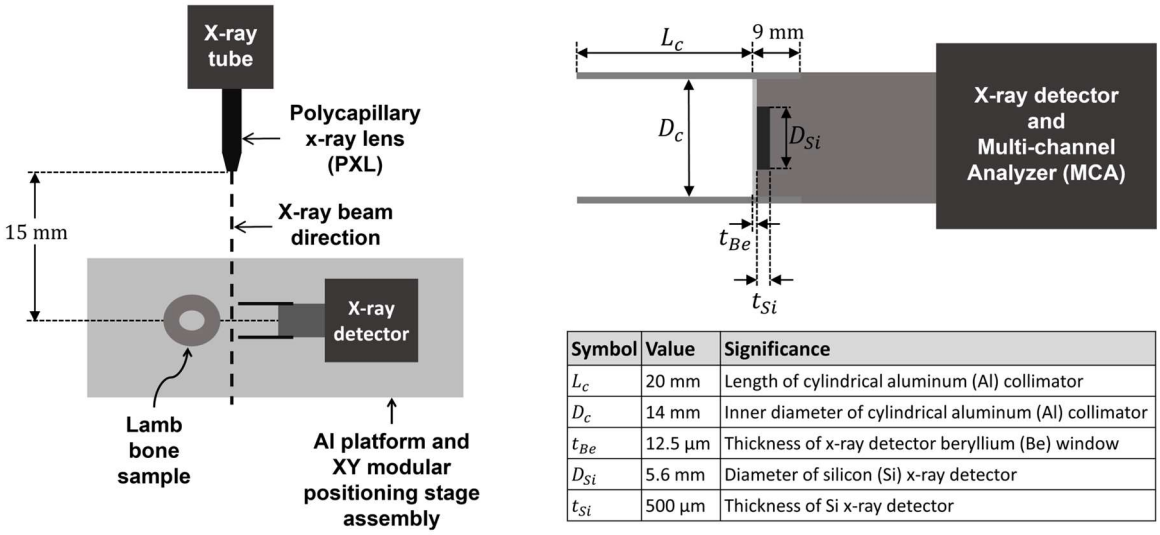

Symbol	Value	Significance
L_c	20 mm	Length of cylindrical aluminum (Al) collimator
D_c	14 mm	Inner diameter of cylindrical aluminum (Al) collimator
t_{Be}	12.5 μm	Thickness of x-ray detector beryllium (Be) window
D_{Si}	5.6 mm	Diameter of silicon (Si) x-ray detector
t_{Si}	500 μm	Thickness of Si x-ray detector

Figure 1. (**a**) view from the top schematic of experimental setup used for lamb bone Sr KXRF measurements. (**b**) detailed cross sectional schematic of the X-ray detector.

The lamb bone sample was positioned on the horizontal Al plate at about 1.7 mm from the Al collimator attached to X-ray detector. The overlying leather and lamb bone sample (see Section 2.1.2.) were placed in the front of the collimator without a gap. Using this setup, the X-ray detector and sample assembly were simultaneously positioned relative to the fixed X-ray beam direction.

The characteristics of the X-ray beam shaped by the PXL are presented in detail in previous publications [61,62]. The focal distance of the PXL was 4 mm. The beam's FWHM at the focal point was measured to be roughly in the 15 μm to 30 μm range in the 8 keV to 30 keV photon energy range. FWHM at the focal point provided by the manufacturer was 24.8 μm at the 9.67 keV photon energy (W Lβ1). The microbeam divergence downstream from the focal point was measured to be about 76 mrad. The FWHM value at distance d from the focal point can be estimated using the following equation:

$$\text{FWHM} = 0.0248 \text{ mm} + 2 \cdot 0.076 \cdot d \quad (1)$$

At the X-ray incidence distance of 15 mm from the PXL, $d = 15 - 4 = 11$ mm, hence, the beam's FWHM was 1.7 mm.

The X-ray beam photon count rate was measured at 15 mm from PXL using X-ray tube settings 50 kV voltage and 0.005 mA current and the aligned X-ray detector. Adjusting for detector's detection efficiency as a function of photon energy (see Equation (21) of Section 2.3.1), Gaussian beam size (FWHM = 1.7 mm) and detector area correction factor of 1.005, and X-ray tube current, the photon rate output of the X-ray tube with the 1.8 mm Al filter at 50 kV and 1 mA was estimated to be 1.1×10^6 photons s^{-1}.

2.1.2. Experimental Samples

A lamb bone was purchased from a local grocery store in Fresno, California, United States. The lamb was likely raised on a local farm, but the precise, origin, feeding routines, age, and other specifics of the animal were not known. The entire lamb bone was extracted by removing skin, muscle, tendons, and bone marrow tissues. Initially, the forensic bone cleaning method of Mairs et al. [63] using detergent maceration was employed, but abandoned after being deemed as inefficient. The lamb bone was subsequently boiled in tap water for about two hours. After allowing cooling of the lamb bone, the remaining tendons, soft tissue, and bone marrow were easily removed, and the bone was subsequently dried. The spongious (or trabecular) bone ends were cut using a band saw. The middle part of the bone of about 4 cm in length was kept intact and was used in the KXRF measurements. The lamb bone (LB) sample mass was measured to be 16.859 ± 0.001 g. Its volume measured by water displacement was 10.0 ± 0.5 cm^3. The average bone density was then calculated to be 1.69 ± 0.08 g cm^{-3}. A view from the top of the LB sample can be seen on the left-hand side of the digital photograph of Figure 2. The other parts were sectioned longitudinally along the length of the bone and then the remaining bone parts were sectioned in thinner slices using a diamond blade saw (model 650, South Bay Technology, Inc., San Clemente, CA, USA). One of the slices of 0.38 ± 0.03 mm thickness was used in lamb bone linear attenuation coefficient measurements and its digital photograph is shown in Figure 2. The minimally-processed leather was purchased from a local store and the larger pieces were cut into smaller pieces. The rectangular leather piece used in the XRF experiments had an area of about 4 cm by 8 cm, 2.80 ± 0.05 mm thickness, and can also be seen in Figure 2.

2.1.3. XRF Experimental Procedures

X-ray spectra were acquired by the X-ray detector during X-ray beam irradiation of the LB and lamb bone with overlying leather (LBOL) which simulated in vivo experimental conditions. The LBOL sample was prepared by tightly wrapping the leather around the lamb bone and securing with elastic bands on the top and bottom ends. The line marked by pen on the top of the lamb bone in Figure 2a indicates the side facing the X-ray detector collimator. The X-ray beam was perpendicular to this line intersecting the sample in a point which was approximately located in the middle of the bone length. In both cases, the sample was positioned at 15 mm from the PXL end as indicated in Figure 1a. At this position, the lateral size of the X-ray beam expressed as FWHM was 1.7 mm [60]. The XRF procedure titled the optimal grazing-incidence position (OGIP) [58–60], was applied to both samples. The OGIP was obtained from data analysis of sequential 10-s duration X-ray spectra acquired at positions separated by equal 0.5 mm steps which brought the sample

closer to the X-ray beam while the detector-sample distance was constant as explained in the previous Section 2.1.1. The initial position was selected such that the X-ray beam was not incident on the sample. The OGIP corresponded to the maximum of the convolution function (Gaussian and exponential functions) fitted to the Sr Kα peak area versus position data [59]. At the optimal position, three 300-s trials were acquired. Ten 0.5 mm steps were required for both LB and LBOL samples.

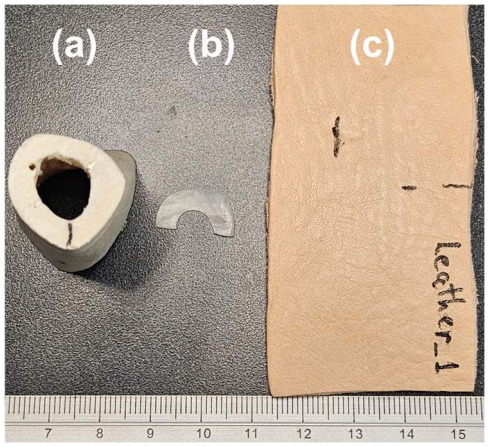

Figure 2. Digital photograph of three samples: (**a**) lamb bone (LB), (**b**) lamb bone slice, and (**c**) overlying leather.

2.1.4. Data Analysis

XRF peaks identified in the X-ray spectra were fitted using the built-in nonlinear curve fitting tool in the OriginPro 2020 data analysis and plotting software (OriginLab, Northampton, MA, USA). Custom fitting functions were written using the Origin nonlinear fitting tool. The fitting functions $f(x)$ were written as the sum of a background represented by a first or second order polynomial functions $P(x)$ and one or two Gaussian functions $G(x; x_i, s_i)$ characterized by peak area A_i, center x_i and standard deviation s_i. An example of fitting function $f(x)$ including $P(x)$ as a first order polynomial and a single Gaussian function $G(x; x_1, s_1)$ is given by the following equation:

$$f(x) = P(x) + G(x; x_1, s_1) = a + bx + \frac{A_1}{s_1\sqrt{2\pi}} \exp\left[-\left(\frac{(x - x_1)^2}{(2{s_1}^2)}\right)\right]. \quad (2)$$

The nonlinear fitting was performed using the statistical weighting option. Thus, the statistical weight of a y-axis value y, was computed as $1/y$ as predicted by the Poisson statistics governing the number of counts recorded in individual channels of the X-ray detector and multi-channel analyzer unit. The goodness-of-fit of multiple peak fittings was done by monitoring the reduced chi-squared (χ^2/n) values. The chi-squared test was performed to determine if χ^2/n were significantly larger than unity. The test was performed using Excel's CHISQ.DIST.RT function which computes the right-tailed probability of the chi-squared distribution. Test results below 5% indicated a χ^2/n value significantly larger than unity. The result of the three 300-s trials was computed as a weighted average and its corresponding weighted error with statistical weights computed as the inverse error squared.

2.2. X-ray Linear Attenuation Coefficient Measurements

The X-ray linear attenuation coefficients of lamb bone slice, leather sample, and Al were measured by employing a procedure described in our previous publication [60]. Comparison of the linear attenuation coefficient measurements of Al to the corresponding values of the XCOM database [63] was used to ensure procedural reliability. In short, samples were positioned at the focal point of the PXL where the beam's FWHM was about

25 μm. The linear attenuation coefficient of the sample at photon energy $\mu(E)$ was derived from the following equation:

$$\mu(E) = [\ln(S(0)/S(t))]/t \quad (3)$$

In Equation (3), t is the sample's thickness, and $S(0)$ and $S(t)$ are measured spectrometric quantities at photon energy E corresponding to beam attenuation by air and by air and sample of thickness t, respectively. Spectrometric quantities were: (i) the areas of the observed L-shell of tungsten (W) peaks and (ii) the average number of counts recorded in 1 keV energy intervals (~50 channels) in the broad bremsstrahlung peak.

2.3. 2D-KXRF Model

2.3.1. Theory

The 2D-KXRF model was based on an elliptical geometrical representation of the LB's transversal cross section. The LBOL sample was represented by an added layer of uniform thickness t_0 as indicated in the schematic of Figure 3. In this representation, the LB shaft was ignored, given that X-ray beam probed LB's elements only a few millimeters in depth. Given the semi-minor and semi-major axes values a and b, the elliptical bone contour is given by:

$$\frac{x^2}{a^2} + \frac{(y - y_0)^2}{b^2} = 1 \quad (4)$$

and the elliptical overlying soft tissue contour is given by:

$$\frac{x^2}{a'^2} + \frac{(y - y_0)^2}{b'^2} = 1 \quad (5)$$

where,

$$a' = a + t_0 \quad (6)$$

$$b' = b + t_0 \quad (7)$$

and,

$$y_0 = L_c + t_0 + b \quad (8)$$

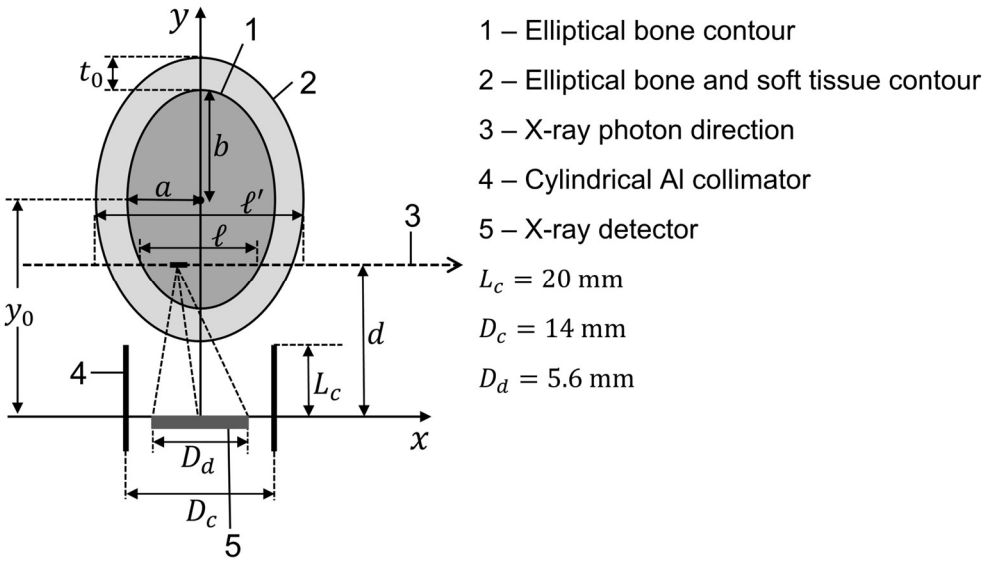

Figure 3. Simplified two-dimensional (2D) elliptical representation of the transversal cross section of the bone and soft tissue XRF experiment described in the text. The incident photon direction is parallel to the X-ray detector surface. The detector center coincides with the origin of the Cartesian axes.

The soft tissue thickness crossed by the X-ray photon on one side before reaching the bone is denoted by t_{st} and is given by:

$$t_{st} = \left(\ell' - \ell\right)/2 \tag{9}$$

Total length along the microbeam in the bone and soft tissue was denoted by ℓ' and in the bone alone by ℓ, as indicated in Figure 3. Setting $y = d$ in the elliptical soft tissue contour equation, one obtains:

$$\ell' = 2a'\sqrt{1 - \left(\frac{y_0 - d}{b'}\right)^2} \tag{10}$$

Similarly, setting $y = d$ in the elliptical bone contour equation, gives:

$$\ell = 2a\sqrt{1 - \left(\frac{y_0 - d}{b}\right)^2} \tag{11}$$

The soft tissue thickness t_{st} is found by plugging the right-hand sides of Equations (10) and (11) in Equation (9):

$$t_{\mathrm{st}} = a'\sqrt{1 - \left(\frac{y_0 - d}{b'}\right)^2} - a\sqrt{1 - \left(\frac{y_0 - d}{b}\right)^2} \tag{12}$$

The absorption of the X-ray photon in the bone tissue occurs between left-hand and right-hand side points of coordinates $\left(-\frac{\ell}{2}, d\right)$ and $\left(\frac{\ell}{2}, d\right)$. Assume a bone element of infinitesimal length $d\ell$ along the photon direction at a position x between the abovementioned points. At position x, it was assumed that the average distance traveled by the XRF photons in the bone, $t_b(x)$, and the average distance traveled in the soft tissue, $t(x)$, are along the line which connects the X-ray detector center $(0, 0)$ and the position (x, d) of element $d\ell$. Exact expressions for $t_b(x)$ and $t(x)$ are cumbersome; approximate expressions can be derived from the triangular geometry of Figure 4. These are:

$$t_b(x) = [d - (L_c + t_0)]/\cos\theta, \tag{13}$$

$$t(x) = t_0/\cos\theta, \tag{14}$$

$$\theta = \tan^{-1}(x/d). \tag{15}$$

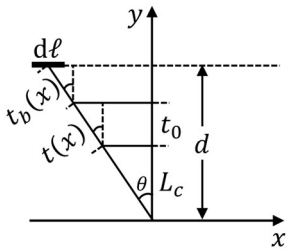

Figure 4. Triangular geometry used for the derivation of the approximate equations for distances in bone $t_b(x)$ and soft tissue $t(x)$ traveled by XRF photons generated in an infinitesimal bone element of length $d\ell$ at position x.

In Equations (13) and (14), one can notice that dependence of $t_b(x)$ and $t(x)$ on the horizontal position x occurs via angle θ indicated in Figure 4 and defined by trigonometric Equation (15).

The solid angle $\Omega(x)$ encompassing all the XRF photons emitted by the element $d\ell$ at position x that are incident on the detector of diameter D_d is approximately given by:

$$\Omega(x) \cong \frac{\pi(D_d/2)^2}{d^2}\cos\theta \tag{16}$$

For a particular chemical element in the bone, the K-shell XRF (KXRF) yield (number of photons, fluence, or fluence rate), is the ratio between the sum of the detected photon output corresponding to KXRF atomic transitions ($I_{\mathrm{K}\alpha} + I_{\mathrm{K}\beta}$) and photon input I_0. The KXRF yield can be separated in two equations by spectroscopically-resolved transitions:

$$\frac{I_{K\alpha}}{I_0} = \int_{E_K}^{E_{\max}} \left\{ S(E)\cdot p_{\mathrm{K}\alpha} \int_{-\frac{\ell}{2}}^{\frac{\ell}{2}} \frac{\Omega(x)}{4\pi}\varepsilon(E_\alpha, x)\exp\left\{-\left[\mu_b(E)\left(x+\frac{\ell}{2}\right) + \mu_{\mathrm{b}}(E_\alpha)t_{\mathrm{b}}(x) + \mu_{\mathrm{st}}(E_\alpha)t(x)\right]\right\}\mathrm{d}x \right\} f(E)\mathrm{d}E \tag{17}$$

$$\frac{I_{K\beta}}{I_0} = \int_{E_{\mathrm{K}}}^{E_{\max}} \left\{ S(E)\cdot p_{\mathrm{K}\beta} \int_{-\frac{\ell}{2}}^{\frac{\ell}{2}} \frac{\Omega(x)}{4\pi}\varepsilon(E_\beta, x)\exp\left\{-\left[\mu_b(E)\left(x+\frac{\ell}{2}\right) + \mu_{\mathrm{b}}(\mathrm{E}_\beta)\mathrm{t}_{\mathrm{b}}(x) + \mu_{\mathrm{st}}(\mathrm{E}_\beta)t(x)\right]\right\}\mathrm{d}x \right\} f(E)\mathrm{d}E \tag{18}$$

In Equations (17) and (18), the quantity $S(E)$ of inverse length dimension is given by:

$$S(E) = c\tau(\mathrm{E})\rho_b V_K \omega_K \exp[-\mu_{\mathrm{st}}(E)t_{\mathrm{st}}] \tag{19}$$

The derivation of Equations (17) to (19) is included in Appendix A. The function $f(E)$ defines the incident photon energy spectrum and is normalized such that:

$$\int_0^{E_{max}} f(E)\mathrm{d}E = 1 \tag{20}$$

Quantities E_{max} and E_K are the maximum incident photon energy and the K-shell absorption edge energy of the chemical element of interest, respectively. Distances ℓ, $t_b(x)$, and $t(x)$ are described above and can be computed using Equations (9) to (15). They are dependent on both position x along the photon direction, but also on the distance d between photon direction and X-ray detector. Quantities $\varepsilon(E_\alpha, x)$ and $\varepsilon(E_\beta, x)$ are the detector's efficiency values at KXRF photon energies E_α and E_β originating from X-ray absorption of sample element of length dx at position x. Position x dependence is indirect through angle θ defined in Equation (15). Detector efficiency at photon energy E and angle θ, $\varepsilon(E, \theta)$, was computed according to the following equation:

$$\varepsilon(E,\theta) = \exp(-\mu_{Be}(E)t_{Be}/\cos\theta)[1-\exp(-\mu_{\mathrm{Si}}(E)t_{\mathrm{Si}}/\cos\theta)] \tag{21}$$

Definitions and values of several of the physical parameters in Equations (17)–(19) are summarized in Table 1.

Table 1. Significance, numerical values, and units of physical parameters which are defined in the text. Notice that the relative Sr Kα and Sr Kβ signals were computed using a unity Sr concentration.

Symbol	Significance	Value/Range	Units	Source
E	Incident photon energy	10–50	keV	Measurement
E_α	Average Kα photon energy	14.1	keV	Deslattes et al. [4]
E_β	Average Kβ photon energy	15.8	keV	Deslattes et al. [4]
ρ_b	Mass density of cortical bone	1.9	g cm^{-3}	
$\tau(E)$	Sr photoelectric mass attenuation coefficient at photon energy E	60.65–49.70	cm^2 g^{-1}	XCOM database [64]
V_K	K-shell vacancy probability for Sr	0.8548	-	Elam et al. [64]
ω_K	K-shell fluorescence yield	0.6647	-	Elam et al. [64]
$p_{K\alpha}$	Relative Kα emission intensity	0.8488	-	Elam et al. [64]
$p_{K\beta}$	Relative Kβ emission intensity	0.1512	-	Elam et al. [64]
$\mu_{st}(E)$	Soft tissue linear attenuation coefficient at photon energies E, E_α, and E_β.	variable	mm^{-1}	Measurement
$\mu_b(E)$	Bone linear attenuation coefficient at photon energies E_α and E_β.	variable	mm^{-1}	Measurement and XCOM database
$\mu_{Be}(E)$	Beryllium (Be) linear attenuation coefficient at photon energy E.	variable	cm^{-1}	XCOM database and Be density: 1.85 g cm^{-3}
$\mu_{Si}(E)$	Silicon (Si) linear attenuation coefficient at photon energy E.	variable	cm^{-1}	XCOM database and Si density: 1.85 g cm^{-3}
t_{Be}	Be detector window thickness	0.00125	cm	Manufacturer
t_{Si}	Si detector thickness	0.05	cm	Manufacturer

2.3.2. Numerical Implementation

A C++ code titled "bone_XRF.cpp" and available in supplementary material S1 was written to compute KXRF yields $I_{K\alpha}/I_0$ and $I_{K\beta}/I_0$ defined in Equations (17) and (18). The code was designed to compute the KXRF yields for chemical elements ranging from silicon (Si) (Z = 14) to strontium (Sr) (Z = 38). The photoelectric mass attenuation coefficient at photon energy E, $\tau(E)$, for these 25 chemical elements was interpolated from the XCOM database [64] replicating their procedure. For photon energies above the K-shell absorption edge, $\tau(E)$ was computed employing a log-log cubic spline interpolation algorithm adapted from the numerical library attached to the Press et al. textbook [65]. Linear interpolation was applied to compute $\tau(E)$ for photon energies below the K-shell absorption edge. As indicated in Table 1, the linear attenuation coefficients of lamb bone and soft tissue (i.e., leather), $\mu_b(E)$ and $\mu_{st}(E)$, were measured. However, within the C++ code, linear attenuation coefficients of tissues or materials could also be computed for any photon energy E in the 1 keV to 100 keV range using the XCOM database elemental mass attenuation coefficients and provided the elemental composition. KXRF fundamental parameters V_K, ω_K, $p_{K\alpha}$, and $p_{K\beta}$ were taken from the FPM database of Elam et al. [64]. Numerical integration over the length variable x of Equations (17) and (18) was performed using the trapezoidal method in which the number points inside the integration interval $(-\ell/2,\ \ell/2)$ was sequentially increased until difference between the integral and its preceding value was $<10^{-8}$(p. 158 in Ref. [65]). The photon energy integration from Equations (17) and (18) was numerically performed as the weighted sum of the integrated function computed at 21 photon energy values. The photon energy E values in the 10 keV to 50 keV range in 2 keV increments and their corresponding weights $w(E)$ are provided in Table 2. The weights add up to unity and were calculated from direct measurements of the X-ray beam (50 kV and 1.8 mm Al filter) with the X-ray detector. The measurements were numerically deconvoluted to remove the detection efficiency and energy dispersive effects on the observed energy spectrum. Details

of these measurements and calculations can be found in reference [66]. The weights $w(E)$ derived from the deconvoluted X-ray beam spectrum are plotted against photon energy E in the plot of Figure 5. The other two superimposed plots are the normalized measured energy spectrum from a 50-kV tungsten X-ray tube (1.2 mm Al inherent filtration) of Bhat et al. [67] and computed energy spectrum using SpekCalc software of the tungsten anode X-ray tube [68] using 50 kV and 1.8 mm Al filtration. Differences between the X-ray beam spectrum used in this study and the other two spectra in Figure 5 are due to the PXL's transmission decreasing with increasing photon energy [69].

Table 2. Numerical values of photon energy E and their corresponding weights $w(E)$.

$E(keV)$	$w(E)$	$E(keV)$	$w(E)$	$E(keV)$	$w(E)$
10	3.15×10^{-5}	24	1.32×10^{-1}	38	1.88×10^{-2}
12	6.91×10^{-4}	26	1.01×10^{-1}	40	1.42×10^{-2}
14	7.27×10^{-3}	28	7.63×10^{-2}	42	1.07×10^{-2}
16	3.78×10^{-2}	30	5.76×10^{-2}	44	8.12×10^{-3}
18	1.02×10^{-1}	32	4.36×10^{-2}	46	6.14×10^{-3}
20	1.57×10^{-1}	34	3.29×10^{-2}	48	4.64×10^{-3}
22	1.61×10^{-1}	36	2.49×10^{-2}	50	3.51×10^{-3}

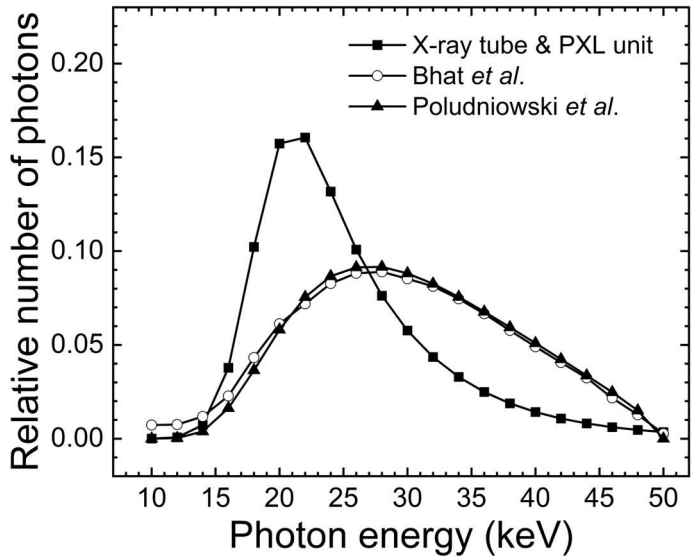

Figure 5. Plots of the energy spectra of X-ray beams generated by the X-ray tube and PXL unit with 1.8 mm added Al filtration used in this study (black full squares) and two spectra of conventional tungsten anode X-ray tube with equivalent Al filtration (black line circles and squares). See text for details [67,68].

The output of the "bone_XRF.cpp" code was a data file representing the KXRF signal from a single incident photon path computed at y-axis values separated by equal steps. A step size of 0.05 mm for the y-axis range of 10 mm (i.e., 200 steps) was selected for Sr Kα and Sr Kβ signals.

The elliptical length parameters a and b of Equation (4) describing the transversal contour of the LB sample were determined as follows. The distance in the bone along a line approximately perpendicular on the marked line at 3 mm from the edge was measured to

be about 10 mm. Therefore, for $y_0 = b$, $x = 5$ mm, and $y = 3$ mm, algebraic manipulation of Equation (4) gives the numerical relationship between a and b (in mm) to be:

$$b = 3 \text{ mm} / \left[1 \pm \sqrt{1 - (5 \text{ mm}/a)^2}\right] \quad (22)$$

Choosing the negative sign solution, numerical value $a = 6.5$ (mm) plugged in the right-hand side of Equation (22), yields $b \cong 8.3$ mm. Figure 6 shows the overlap of the ellipse with these parameters and the digital photograph of the LB's transversal cross section. These a and b values were used as input values in the "bone_XRF.cpp" C++ code described above.

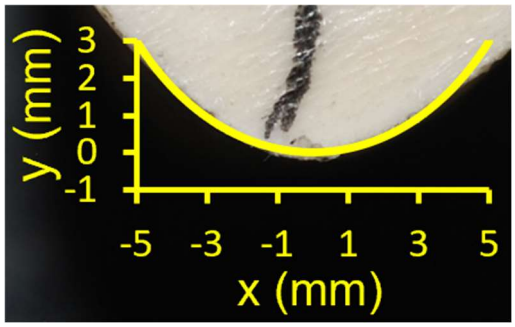

Figure 6. The plot of the ellipse (thick yellow line) overlapped over the digital photograph of LB's cross section.

A separate C++ code named "convolution.cpp" included in the Supplementary Material S2 was written to perform the numerical convolution between the KXRF signal computed from a single incident photon path and normalized Gaussian weights representing the Gaussian profile of the incident X-ray beam generated by the X-ray tube and PXL unit. The output of the "convolution.cpp" code was a file containing the computed the Sr Kα and Sr Kβ signals generated in the bone tissue by the incident Gaussian X-ray beam. The "bone_XRF.cpp" code took 20 s to produce 200 Sr Kα and Sr Kβ signals from as many photon paths in the bone using a laptop computer with a central processing unit (CPU) speed of 1.5 GHz and random access memory (RAM) of 8.00 GB. The convolution C++ code "convolution.cpp" took less than 1 s to produce its results.

3. Results

3.1. XRF Measurements

The OGIP procedure detailed in Section 2.1.3. was employed to find the best position of the sample relative to that of the X-ray beam. Samples of the 300-s X-ray spectra obtained at the optimal position from the LB and LBOL samples are provided in the two plots of Figure 7. The Sr Kα peak area data obtained from the OGIP method is shown in the two plots of Figure 8. One can notice that the calcium (Ca) KXRF peaks cannot be observed in LBOL spectrum of Figure 7b; their characteristic low-energy photons (3.7 keV and 4.0 keV) being completely attenuated by the overlying 2.8-mm leather. The results of the peak fitting routines applied to the 300-s acquired LB and LBOL X-ray spectra are summarized in Table 3. It is important to note that the observed zinc (Zn) KXRF lines origin is from expected trace concentrations of this element in bone. However, contributions from absorption of scattered X-rays by Zn atoms present in some metallic parts of the experimental setup (X-ray detector, PXL) was not excluded and it was observed in other experiments. Bromine (Br) was present in the leather and its origin is linked to the chemical treatment of the animal skin.

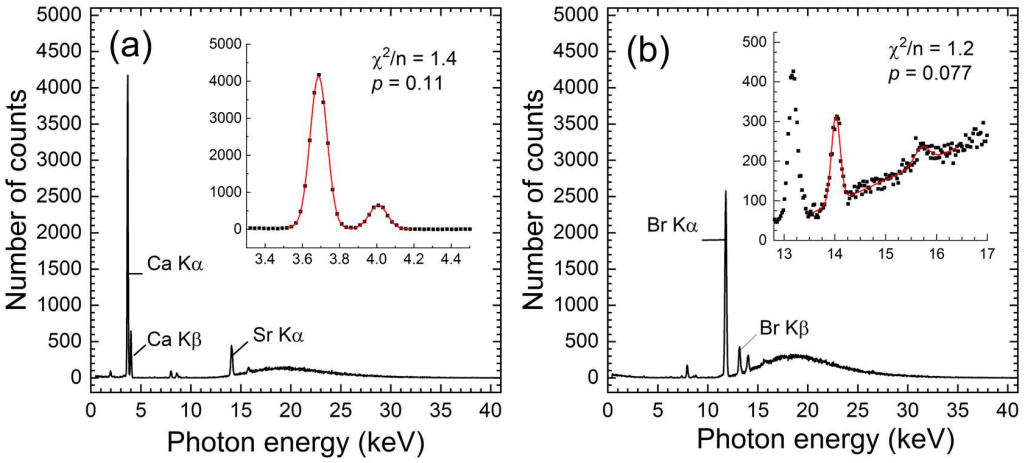

Figure 7. X-ray spectra from the: (**a**) LB and (**b**) LBOL samples (continuous black lines through the 2048 data points); continuous red lines in the insert plots are Gaussian fits to the Ca and Sr KXRF data points (black squares), respectively.

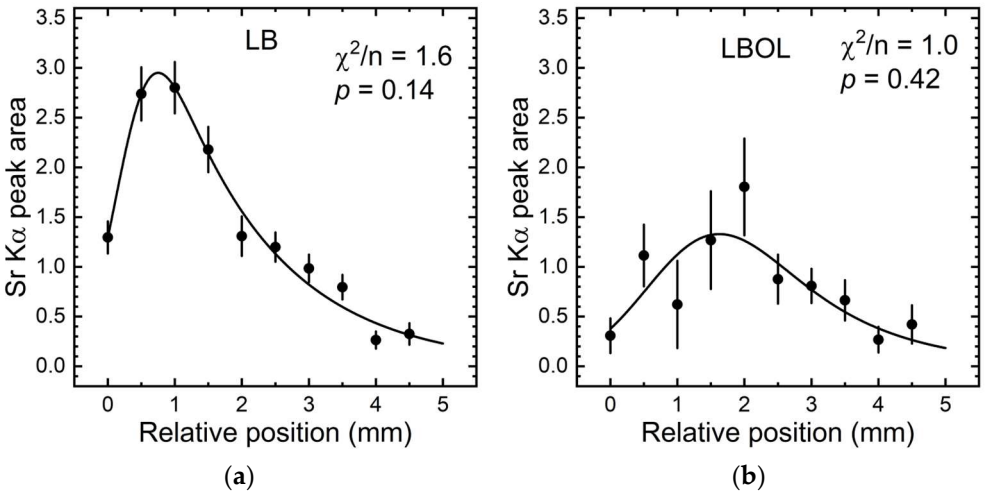

Figure 8. Sr Kα peak area data plots (full black circles) obtained from the OGIP method for the LB (**a**) and the LBOL (**b**) samples. In each plot, the solid black line is the convolution function fit to the data as explained in the text.

Table 3. Summary of peak fitting results corresponding to the 300-s X-ray spectra of the LB and LBOL samples.

LB		**LBOL**	
XRF Peak	**Peak Area**	**XRF Peak**	**Peak Area**
P Kα	11.3 ± 0.5	Zn Kα	3.3 ± 0.2
S Kα	2.1 ± 0.4	Zn Kβ	0.7 ± 0.1
K Kα	0.9 ± 0.4	Br Kα	518 ± 3
Ca Kα	475 ± 2	Br Kβ	81 ± 1
Ca Kβ	77.9 ± 0.9	Sr Kα	49 ± 1
Zn Kα	10.8 ± 0.3	Sr Kβ	10 ± 1
Zn Kβ	1.8 ± 0.2		
Sr Kα	89 ± 1		
Sr Kβ	15.1 ± 0.8		

3.2. Linear Attenuation Coefficients Measurements

A graphical display of the measured linear attenuation coefficients of Al, leather, and lamb bone (LB) in mm^{-1} is provided in log-log plots of Figure 9. Plots (a) to (c) of Figure 9 correspond to Al, leather, and LB measurements, respectively. The continuous lines are linear fittings to the log-log data. The *x*-axis photon energy range was about 7 keV to 20 keV. Plots (d) to (e) compare the best fit lines shown in plots to (a) to (c) to the corresponding values of Al XCOM database [63] values, average human skin, and human cortical bone. The *x*-axis photon energy range in these plots is 2 keV to 50 keV.

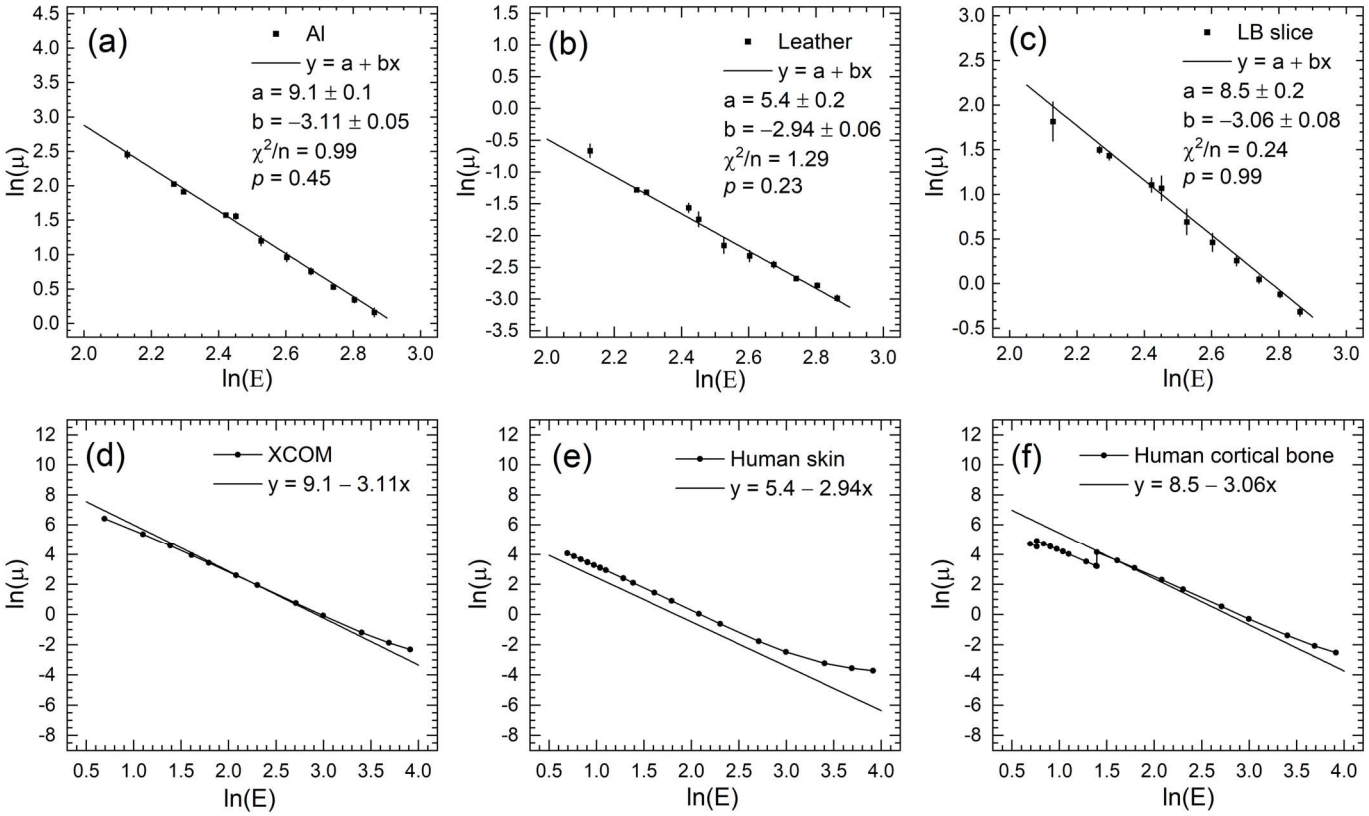

Figure 9. Plots (**a**–**c**) show natural logarithm of the measured linear attenuation coefficient (μ) in mm^{-1} units versus natural logarithm of photon energy (E) in keV units. Plots (**d**–**f**) allow a visual comparison of the measured μ with XCOM data for aluminum (Al) and similar human tissues.

The linear attenuation coefficient values of the average human skin were computed using skin's average elemental composition and 1.09 g cm^{-3} density from report 44 of the International Commission on Radiation Units and Measurements (ICRU) [70] and atomic mass attenuation coefficients from the XCOM database [63]. Similarly, the linear attenuation coefficient values average of the human cortical bone were computed using the average elemental composition and 1.9 g cm^{3} density of human cortical bone from Zhou et al. [71] paper and the XCOM database [63]. The human cortical bone density of Zhou et al. [71] is larger than the measured average LB density of 1.69 ± 0.08 g cm^{-3} mentioned in Section 2.1.2. The difference is likely because the LB sample also contained the less dense trabecular bone tissue.

3.3. 2D-KXRF Model Output

The relative Sr signal from the 2D-KXRF model described in Section 2.3 as a function of *y*-axis position is provided in the four plots of Figure 10. As shown in Figure 3, the *y*-axis is used to quantify the variable position of the incident X-ray photon relative to the sample, X-ray detector, and collimator assembly. Figure 10a,b represent the Sr Kα

and Sr Kβ relative signals versus *y*-axis position of a single incident photon direction, respectively. Figure 10c,d represent the Sr Kα and Sr Kβ relative signals versus the *y*-axis position of a Gaussian X-ray beam direction. Data of Figure 10a,b was computed from data plotted in Figure 10c,d employing the numerical convolution algorithm described in the last paragraph of Section 2.3.2. Numerical values of the Sr signals at several *y*-axis values were graphically interpolated from the Figure 10 plots using OriginPro 2020 tools and are provided in Table 4 at three significant figures precision.

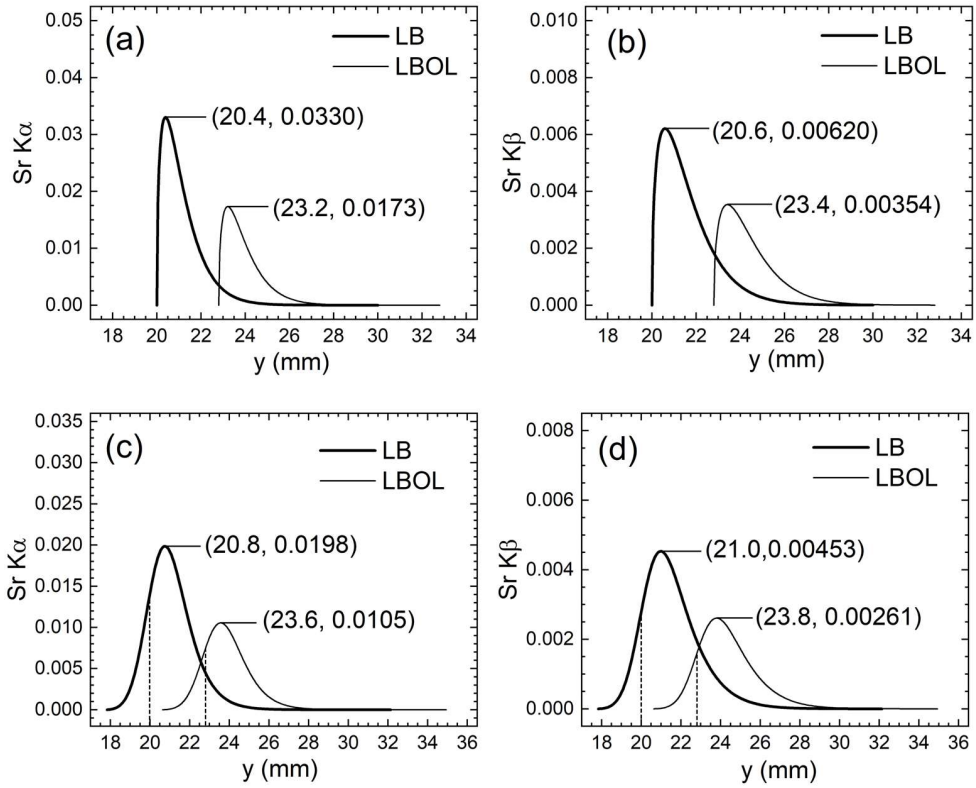

Figure 10. Plots of the Sr Kα and Sr Kβ relative signals versus *y*-axis positions corresponding to the LB (thick black lines) and LBOL (thin black lines) samples. Sr KXRF signals from a single X-ray photon direction are provided in plots (**a**,**b**), and from an X-ray beam in plots (**c**,**d**). The shift to the right of the LBOL curves is due to the 2.8 mm-thick leather layer.

Table 4. Values of the relative Sr Kα and Sr Kβ signals at ten positions of the X-ray photon path and central X-ray beam direction along the *y*-axis. The "edge" denotes *y*-axis positions for which the X-ray photon path is tangent to the elliptical bone contour. The "max" denotes the maximum value.

Sample	*y*-Axis Position (mm)	X-ray Photon		X-ray Beam	
		Sr Kα	Sr Kβ	Sr Kα	Sr Kβ
LB	20.0	0.0000 (edge)	0.00000 (edge)	0.0140 (edge)	0.00275 (edge)
	20.4	0.0330 (max)	0.00602	0.0185	0.00387
	20.6	0.0313	0.00620 (max)	0.0196	0.00425
	20.8	0.0280	0.00605	0.0198 (max)	0.00446
	21.0	0.0240	0.00571	0.0193	0.00453 (max)
LBOL	22.8	0.0000 (edge)	0.0000 (edge)	0.00748 (edge)	0.00161 (edge)
	23.2	0.0173 (max)	0.00341	0.00980	0.00220
	23.4	0.0165	0.00354 (max)	0.0104	0.00242
	23.6	0.0151	0.00346	0.0106 (max)	0.00256
	23.8	0.0130	0.00328	0.0103	0.00261 (max)

The peak shape of the Sr KXRF signals curves is the effect of two opposite processes. An increased KXRF photon production is the result of a longer photon path in the bone. This process is counteracted by the bone and leather attenuation of incident and emergent Sr X-rays. From Figure 10 plots and Table 4 values, one can observe that the distance between the bone tip (or 'edge') and the position corresponding to the maximum signal is higher for Sr Kβ than for Sr Kα. This effect is due to Sr Kβ photons having higher energy (15.8 keV) than their Sr Kα counterparts (~14.1 keV), thus, being less attenuated by the sample before reaching the detector.

3.4. Comparison between 2D-KXRF Model and Experimental Results

The attenuation of the Sr X-rays by the overlying 2.8-mm-thick leather was correctly predicted by the 2D-KXRF model as can be seen by an inspection of the attenuation values of Sr X-rays provided in the fifth row of Table 5. The values predicted by the 2D-KXRF model are within the 95% confidence interval determined by the measured values and their uncertainties.

Table 5. The attenuation of bone Sr X-rays by the overlying 2.8-mm-thick leather. Sr Kα and Sr Kβ attenuation values for measurement, 2D-KXRF model, and exponential attenuation calculations are given in the last row.

Sample	**Sr Kα**			**Sr Kβ**		
	Measurement	**2D-KXRF Model**	**exp**$(-\mu t)$	**Measurement**	**2D-KXRF Model**	**exp**$(-\mu t)$
LBOL	49± 1	0.0106		10 ± 1	0.00256	
LB	89 ± 1	0.0198		15.1 ± 0.8	0.00446	
LBOL/LB	0.55 ± 0.01	0.535	0.772 ± 0.004	0.66 ± 0.07	0.574	0.831 ± 0.003

In Table 5, μ is the X-ray linear attenuation coefficient of leather with values of 0.0926 mm^{-1} and 0.0662 mm^{-1} at 14.1 keV and 15.8 keV Sr X-ray energies, respectively. These values were computed using the linear fit parameters provided in the log-log plot of Figure 9b. The measurement value of 2.80 ± 0.05 mm was given to the leather thickness denoted by t. The error on the exponential attenuation factor, $\exp(-\mu t)$, was computed by applying the general error propagation formula to the uncertainty on thickness t [72]. It is also important to note that the 2D-KXRF model Sr Kβ values for LB and LBOL samples are not the maximum values indicated in Table 4, but correspond to the y-axis positions of the maximum Sr Kα signal to reproduce the experimental XRF procedures described in Section 2.1.3. The attenuation factors predicted by the simple leather exponential attenuation of Sr X-rays are higher than their measurement and model counterparts. The explanation bears on two facts. First, the attenuation of incident X-rays by the overlying soft tissue results in a reduced Sr KXRF production compared to that of the bare bone experiment. Second, the average path length of Sr photons in leather is, on average, larger than its thickness.

The measured Sr Kβ/Kα ratios corrected for detection efficiency and model-based values for LB and LBOL samples are provided in Table 6. These values can be compared to the measured Sr Kβ/Kα atomic ratio 0.181 ± 0.009 of Ertuğral et al. [73] and 0.1781 value computed as the ratio of the relative intensities from Elam et al. [64] database included in Table 1. The corrected experimental ratio for LB sample is slightly lower than the model's computed value.

Table 6. Table of Sr Kβ/Kα ratios. Corrected experimental and model-based values are comparable.

Sample	**(Sr Kβ/Kα)$_{exp}$**	**ε(Kα)/ε(Kβ)**	**(Sr Kβ/Kα)$_{exp}$·ε(Kα)/ε(Kβ)**	**Model**
LB	0.170 ± 0.009	1.19965	0.20 ± 0.01	0.225
LBOL	0.20 ± 0.02	1.19965	0.24 ± 0.02	0.240

Superpositions of the normalized Sr Kα peak area data for the LB and LBOL samples (Figure 7 plots) and their model-based values as a function of X-ray beam position are shown in the two plots of Figure 11. The normalization was performed by dividing each of the experimental and model data sets by its largest value.

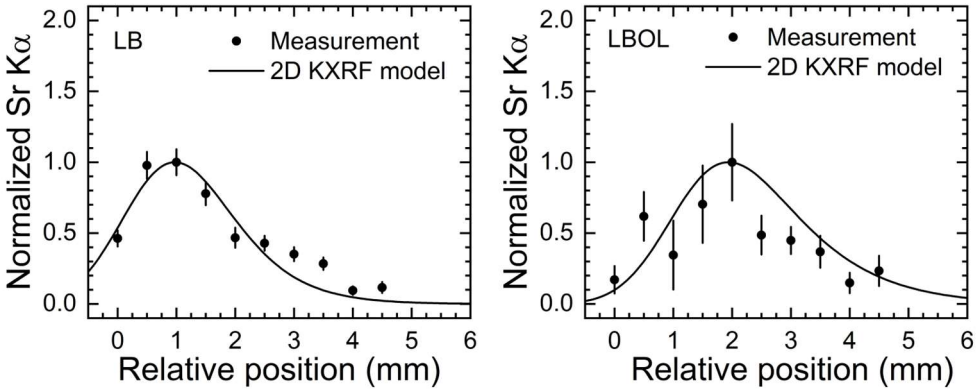

Figure 11. Plots of the normalized measured Sr Kα peak area data (black disks) and the corresponding normalized 2D-KXRF model (black line) versus the relative X-ray beam position. Left and right plots are for LB and LBOL samples, respectively.

3.5. Sr Concentration Estimates

Sr concentration, c, can be estimated by rewriting Equations (17) and (18) as:

$$c = \frac{N_{K\alpha}}{N_0} \cdot \frac{1}{Sr\ K\alpha\ signal}\ , \tag{23}$$

$$c = \frac{N_{K\beta}}{N_0} \cdot \frac{1}{Sr\ K\beta\ signal} \tag{24}$$

In Equations (23) and (24), Sr Kα and Sr Kβ signals were extracted from Table 4 and corresponded to the OGIP X-ray beam positions which were 20.8 mm and 23.6 mm for LB and LBOL samples, respectively. Quantities N_0 $N_{K\alpha}$, and $N_{K\beta}$ denoted the number of incident photons and number of detected Sr Kα and Sr Kβ photons, respectively. The number of incident photons was computed as the X-ray beam count rate of 1.1×10^6 photons/s multiplied by the 300-s acquisition time, giving an estimate of $N_0 \approx 3.3 \times 10^8$ photons. $N_{K\alpha}$ and $N_{K\beta}$ were computed as their respective measured peak areas divided by the 24.6 eV or 0.0246 keV energy per channel determined by the energy calibration of the detector. Table 7 summarizes Sr concentration calculations.

Table 7. Estimates of Sr mass concentration in cortical lamb bone from KXRF measurements and 2D-KXRF model.

Sample	N_0	$N_{K\alpha}$	*Sr Kα Signal*	**c (g g^{-1})**
LB	3.3×10^8	$(3.62 \pm 0.04) \times 10^3$	0.0198	$(5.54 \pm 0.06) \times 10^{-4}$
LBOL		$(1.99 \pm 0.04) \times 10^3$	0.0106	$(5.7 \pm 0.1) \times 10^{-4}$
Sample	N_0	$N_{K\beta}$	*Sr Kβ signal*	
LB	3.3×10^8	$(61 \pm 4) \times 10$	0.00446	$(4.1 \pm 0.3) \times 10^{-4}$
LBOL		$(41 \pm 4) \times 10$	0.00256	$(4.8 \pm 0.4) \times 10^{-4}$

The concentration of Sr in the measured LB sample was not known. However, the estimated Sr bone concentration of about 0.5 mg Sr per gram of cortical bone indicated by the values in the last column of Table 7 is likely an overestimate of the true value. Pejović-Milić et al. [74] gave a range of Sr concentrations in human bone of 0.1 mg to 0.3 mg per

gram of Ca. Using the approximate Ca concentration in human cortical bone of 0.22 g per gram of bone [72], the Sr concentration range can be converted to about 0.02 mg to 0.07 mg per gram of cortical bone. These values are also in line with reported Sr concentrations in cortical bone around 0.05 mg/g reported in the particle-induced X-ray emission (PIXE) study of Zamburlini et al. [75].

4. Discussion

This section will focus on two main topics: (i) limitations of the 2D-KXRF model, (ii) future developments and applications to in vivo XRF measurements. There are two important limitations of the 2D-KXRF model described in this paper, namely (a) dimensionality, and (b) secondary XRF. Radiation-based investigations are intrinsically three-dimensional (3D). The 2D approach greatly simplify certain geometrical computations of the incoming incident X-ray photons and outgoing scattered and fluorescent X-rays. Simulating the XRF produced from a single photon path is still useful, however, one can visualize that the intersection volume between a Gaussian beam and an elliptical cylinder approximating the superficial cortical bone is more complicated than the single-photon-convolution approach included in the 2D-KXRF model. The 2D approach shown in Figure 3 is just a cross section of this interaction volume. X-ray beam photon fluence rate can be represented by a 2D-Gaussian function. Hence, the "weighing" of the single X-ray paths KXRF yield in the bone can be derived from a double convolution along the two Cartesian axes perpendicular to the X-ray beam direction. A negative effect of the 2D approximation seems to be an overestimation of Sr X-rays attenuation within the bone. That would explain the experimental Sr Kβ/Kα ratio being slightly lower than the model's predicted value. A related effect is the likely Sr concentration overestimate which implies low values of Sr Kα and Sr Kβ signals in Equations (23) and (24).

A second important approximation is neglecting secondary XRF emissions in the model. Secondary XRF photons are emitted following photoelectric effect absorption of all scattered photons and characteristic photons emitted by other surrounding atoms and having energies larger than that of shell or subshell edge (i.e., atomic electron binding energy) of the element of interest. For KXRF measurement of bone Sr, there are no other elements with XRF photon energies larger than the Sr K-edge ~16.1 keV [4]. Secondary XRF contribution due to scattered X-rays can be looked at by analyzing the average fraction of scattering events along a primary photon path of length L. This average fraction will depend on L and on the ratio between the combined scattering mass attenuation coefficient, $(\sigma_{coh} + \sigma_{incoh})/\rho$, and the total mass attenuation coefficient, μ/ρ. Figure 12 shows $(\sigma_{coh} + \sigma_{incoh})/\mu$ percentage ratio versus photon energies in the 1 to 100 keV range and four different human tissues. Average elemental compositions of human cortical bone and dentin were taken from references [71] and [76], respectively; the elemental compositions of human skin and adipose tissue was taken from reference [70]. All mass attenuation coefficients were computed using the online XCOM database [63].

Figure 12 plot shows that $(\sigma_{coh} + \sigma_{incoh})/\mu$ percentage ratio is about 10% or lower at photon energies below 20 keV and larger than 50% at photon energies larger than 50 keV for tissues with high-Z elements such as cortical bone and tooth's dentin. For soft tissues such as human skin and adipose tissue containing low-Z atoms, $(\sigma_{coh} + \sigma_{incoh})/\mu$ percentage ratio is larger than 40% for photon energies above 20 keV. Most of photon energies in the X-ray beam used in this study were below 30 keV as can be seen in the spectrum plot of Figure 3. Therefore, neglecting bone Sr KXRF contributions from scattered X-rays is a reasonable approximation. This conclusion is not valid in models or MC simulations of elemental XRF investigations of soft tissues.

Additional work will be required to include a 3D geometrical approach in the current model. Modifications aimed at modeling KXRF experiments using broader X-ray beams or point sources will enhance its range of applications. Inclusion of scattered photons and secondary XRF will naturally lead to employment of MC methods to maintain or improve current speed. At all steps of future developments, an effort will be made not

to reproduce existing codes and numerical approaches. A balance between analytical and numerical approaches will be the key to develop dedicated, accurate, and fast codes centered on applications. Fast and user-friendly codes can be employed to investigate the XRF signal dependence on several parameters that are typically unknown during in vivo experimental conditions such as bone and overlying tissue size and shape and linear attenuation coefficients.

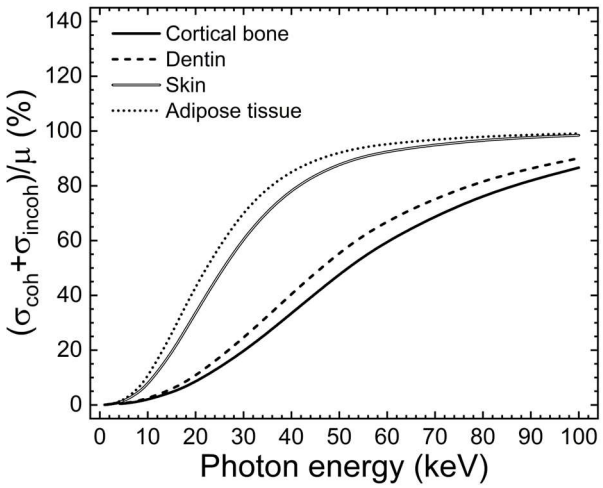

Figure 12. Plot of the $(\sigma_{coh} + \sigma_{incoh})/\mu$ ratio versus photon energy for four human tissues indicated in the legend.

KXRF signal of Ca observed in the XRF experiments (see Table 3) was also modeled employing the 2D-KXRF model. For brevity reasons, the results are not included in this paper. A stronger argument for not including the Ca results can be invoked. The extrapolation of the lamb bone best line fit to the low Ca KXRF energies of 3.7 keV and 4.0 keV will yield incorrect results due to the Ca K-edge at 4.05 keV photon energy [4] as can be seen in Figure 9f plot. Ongoing effort is also taken to apply the current model to Sr measurements in plaster-of-Paris ($CaSO_4 \cdot 2H_2O$) bone phantoms in which the Sr concentration was measured as 1.01 ± 0.07 mg g^{-1} [60].

5. Conclusions

A two-dimensional model named 2D-KXRF was developed to compute the K-shell XRF signal of trace elements in bone. Bone contour and overlying soft tissue of constant thickness were modelled as elliptical curves. In the framework of the fundamental parameter method, the KXRF signal was computed as the sum of KXRF contributions from photon absorption in bone elements of small length along the photon path in the bone. Sample attenuation of incident and emergent photons, detector efficiency, and energy spectrum of incident photons were accounted for. The excitation-detection geometry was reproduced and Sr KXRF signals for a parallel Gaussian X-ray beam were given by a numerical convolution. The model's predictions were tested against Sr KXRF measurements from a lamb bone (LB) and a lamb bone with overlying leather (LBOL). The model's predictions of the attenuation of Sr Kα (14.1 keV) and Sr Kβ (15.8 keV) photons due to the overlying leather agreed with measurements. 2D-KXRF model's prediction of the Sr Kβ/Kα for the LBOL sample also agreed with its measured value corrected for detector's efficiency, but model's predicted value for the LB sample was slightly larger than its measured value. To the best knowledge of the author, this is the first detailed model accurately predicting combined bone and soft tissue attenuation of Sr X-rays and opens the door for future work on finding bone elemental concentrations from in vivo XRF measurements.

Supplementary Materials: The following supporting information can be downloaded at: https://www.mdpi.com/article/10.3390/metrology3040020/s1, Figure S1: Three-trial X-ray spectra obtained in the X-ray attenuation measurements in the 8 keV to 18 keV photon energy range. Attenuated spectra from each sample can be visually compared to that of air provided in the upper-left corner; Figure S2: Sample plots of the X-ray spectra acquired in 10-second intervals at different positions of the lamb bone (LB) and lamb bone with overlying leather (LBOL) samples relative to the X-ray beam. Two separate photon energy intervals are shown focusing on Ca KXRF peaks (left) and Sr KXRF peaks (right). Experimental X-ray spectra data file titled Raw data.xlsx and C++ codes: bone_XRF.cpp and convolution.cpp are also provided

Funding: This research received no external funding.

Data Availability Statement: The data presented in this study can be found within the article or in the supplemental materials.

Acknowledgments: The author would like to acknowledge Michelle Berrios for procurement of the leather samples used in this study.

Conflicts of Interest: The author declares no conflict of interest.

Appendix A

The derivation of Equations (17) to (19) is based on Figure 3 schematic and the fundamental parameter approach which follows mathematically atomic processes and interactions leading to XRF production. Let us assume an incident photon travelling in a direction parallel with the X-ray detector and x-axis and having an energy between the K-edge energy E_K of the bone element (Sr has a K-edge of 16.107 keV) and the maximum X-ray beam energy (50 keV for the X-ray beam used in this study). Let us assume an infinitesimal bone element of length dx along the incident photon's path at Cartesian coordinates x and $y = d$ as shown in Figure 3 schematic. The bone depth is then $x + \ell/2$, where ℓ is the bone total thickness in the photon's direction at distance d from the X-ray detector. Hence, bone depth along photon's path varies from 0 to ℓ for x values between $-\ell/2$ and $+\ell/2$. The photon's probability in reaching bone element dx is given by its attenuation in the bone along $x + \frac{\ell}{2}$ depth and in leather expressed by: $\exp\left[-\mu_b(E)\left(x + \frac{\ell}{2}\right) - \mu_{st}(E)t_{st}\right]$, where $\mu_b(E)$ and $\mu_{st}(E)$ are the linear attenuation coefficients of the photon in bone and soft tissue, respectively. Soft tissue thickness in photon's path was denoted by t_{st}. The probability of the incident photon being absorbed in a photoelectric effect event within the bone element is given by: $c\ \rho_b \tau(E)\ \mathrm{d}x$, where c is the concentration by mass of the bone's chemical element under investigation (Sr in this case), $\tau(E)$ denotes its photoelectric part of the mass attenuation coefficient, and ρ_b is bone mass density. Further, the probability of a Kα photon emission following the photoelectric absorption event is $c\ \rho_b \tau(E)\ V_K\ \omega_K p_{K\alpha} \mathrm{d}x$. V_K , ω_K, and $p_{K\alpha}$ denote the probability of a K-shell vacancy, the K-shell fluorescence yield, and the probability of a Kα photon emission, respectively. Only a fraction equal to $\Omega(x)/4\pi$ out of all isotropically emitted Kα photons can reach the detector. Further reductions of the detected Kα photons occur due to bone and soft tissue attenuations expressed by: $\exp[-\mu_b(E_\alpha)t_b(x) + \mu_{st}(E_\alpha)t(x)]$ and detector's efficiency $\varepsilon(E_\alpha, x)$. Detector's efficiency dependence on bone element position x indicates variation of the path length of Kα photon as it crosses the X-ray detector determined by its original position and direction. A similar treatment yields a fraction of the detected Kβ photon emissions. Integration over position variable x and photon energy E completes the calculations of relative detected Kα and Kβ photons.

References

1. Hall, T. X-ray fluorescence analysis in biology. *Science* **1961**, *134*, 449–455. Available online: http://www.jstor.org/stable/1707782 (accessed on 22 May 2023). [CrossRef] [PubMed]
2. Mattson, S.; Börjesson, J. X-ray fluorescence in medicine. *Spectrosc. Eur./World* **2008**, *20*, 15–17.
3. Chettle, D.R.; McNeill, F.E. Elemental analysis in living human subjects using biomedical devices. *Physiol. Meas.* **2019**, *40*, 12TR01. [CrossRef] [PubMed]

4. Deslattes, R.D.; Kessler, E.G.; Indelicato, P.; de Billy, L.; Lindroth, E.; Anton, J. X-ray transition energies: New approach to a comprehensive evaluation. *Rev. Mod. Phys.* **2003**, *75*, 35–90. [CrossRef]
5. Malmstrom, B.G.; Neilands, J.B. Metalloproteins. *Annu. Rev. Biochem.* **1964**, *33*, 331–354. [CrossRef] [PubMed]
6. Shi, W.; Chance, M.R. Metallomics and metalloproteomics. *Cell. Mol. Life Sci.* **2008**, *65*, 3040–3048. [CrossRef]
7. Waldron, K.J.; Rutherford, J.C.; Ford, D.; Robinson, N.J. Metalloproteins and metals sensing. *Nature* **2009**, *460*, 823–830. [CrossRef]
8. Hoffer, P.B.; Jones, W.B.; Crawford, W.B.; Beck, R.; Gottschalk, A. Fluorescent thyroid scanning: A new method of imaging the thyroid. *Radiology* **1968**, *90*, 342–344. [CrossRef]
9. Ahlgren, L.; Lidén, K.; Mattson, S.; Tejning, S. X-ray fluorescence analysis of lead in human skeleton in vivo. *Scand. J. Work. Environ. Health* **1976**, *2*, 82–86. Available online: https://www.jstor.org/stable/40964582 (accessed on 29 September 2015). [CrossRef]
10. Somervaille, L.J.; Chettle, D.R.; Scott, M.C. In vivo measurement of lead in bone using x-ray fluorescence. *Phys. Med. Biol.* **1985**, *30*, 929–943. [CrossRef]
11. Keldani, Z.; Lord, M.L.; McNeill, F.E.; Chettle, D.R.; Gräfe, J.L. Coherent normalization for in vivo measurements of gadolinium in bone. *Physiol. Meas.* **2017**, *38*, 1848–1858. [CrossRef] [PubMed]
12. Nie, H.; Chettle, D.; Luo, L.; O'Meara, J. In vivo investigation of a new ^{109}Cd γ-ray induced K-XRF bone lead measurement system. *Phys. Med. Biol.* **2006**, *51*, 351–360. [CrossRef] [PubMed]
13. Wielopolski, L.; Rosen, J.F.; Slatkin, D.N.; Vartsky, D.; Ellis, K.J.; Cohn, S.H. Feasibility of noninvasive analysis of lead in human tibia by soft x-ray fluorescence. *Med. Phys.* **1983**, *10*, 248–251. [CrossRef] [PubMed]
14. Zamburlini, M.; Pejović-Milić, A.; Chettle, D.R. Coherent normalization of finger strontium XRF measurements: Feasibility and limitations. *Phys. Med. Biol.* **2008**, *53*, N307. [CrossRef] [PubMed]
15. Nguyen, J.; Crawford, D.; Howarth, D.; Sukhu, B.; Pejović-Milić, A.; Gräfe, J.L. Ex vivo quantification of lanthanum and gadolinium in post-mortem human tibiae with estimated barium and iodine concentrations using K x-ray fluorescence. *Physiol. Meas.* **2019**, *40*, 085006. [CrossRef]
16. Nguyen, J.; Pejović-Milić, A.; Gräfe, J.L. Investigating coherent normalization and dosimetry for the Am-La K XRF system. *Physiol. Meas.* **2020**, *41*, 075014. [CrossRef]
17. Sherman, J. The theoretical derivation of fluorescent X-ray intensities from mixtures. *Spectrochim. Acta* **1955**, *7*, 283–306. [CrossRef]
18. Van Dyck, P.M.; Török, S.B.; Van Grieken, R.E. Enhancement effect in x-ray fluorescence analysis of environmental samples of medium thickness. *Anal. Chem.* **1986**, *58*, 1761–1766. [CrossRef]
19. Nielson, K.K. Matrix corrections for energy dispersive x-ray fluorescence analysis of environmental samples with coherent/incoherent scattered x-rays. *Anal. Chem.* **1977**, *49*, 641–648. [CrossRef]
20. He, F.; Van Espen, P.J. General approach for quantitative energy dispersive x-ray fluorescence analysis based on fundamental parameters. *Anal. Chem.* **1991**, *63*, 2237–2244. [CrossRef]
21. Sprang, V.; Bekkers, M.H.J. Determination of light elements using x-ray spectrometry. Part I—Analytical implications using scattered tube lines. *X-ray Spectrom.* **1998**, *27*, 31–36. [CrossRef]
22. Wegrzynek, D.; Markowicz, A.; Chinea-Cano, E. Application of the backscattered fundamental parameter method for in situ element determination using a portable energy-dispersive x-ray fluorescence spectrometer. *X-ray Spectrom.* **2003**, *32*, 119–128. [CrossRef]
23. Bos, M.; Vrielink, J.A.M. Constraints, iteration schemes and convergence criteria for concentration calculations in X-ray fluorescence spectrometry with the use of the fundamental parameter methods. *Anal. Chim. Acta* **1998**, *373*, 291–302. [CrossRef]
24. Kitov, B.I. Calculation features of the fundamental parameter method in XRF. *X-ray Spectrom.* **2000**, *29*, 285–290. [CrossRef]
25. Szalóki, I.; Gerényi, A.; Radócz, G.; Lovas, A.; De Samber, B.; Vincze, L. FPM model calculation for micro X-ray fluorescence confocal imaging using synchrotron radiation. *J. Anal. At. Spectrom.* **2017**, *32*, 334–344. [CrossRef]
26. Malzer, W.; Kanngießer, B. Calculation of attenuation and X-ray fluorescence intensities for non-parallel x-ray beams. *X-ray Spectrom.* **2003**, *32*, 106–112. [CrossRef]
27. Vasquez, R.P. Composition determination for complex and transmitting samples in x-ray quantitative analysis. *X-ray Spectrom.* **2008**, *37*, 599–602. [CrossRef]
28. Barrea, R.A.; Bengió, S.; Derosa, P.A.; Mainardi, R.T. Absolute mass thickness determination of thin samples by X-ray fluorescence analysis. *Nucl. Instrum. Methods Phys. Res. B* **1998**, *143*, 561–568. [CrossRef]
29. Fiorini, C.; Gianoncelli, A.; Longoni, A.; Zaraga, F. Determination of the thickness of coatings by means of a new XRF spectrometer. *X-ray Spectrom.* **2002**, *31*, 92–99. [CrossRef]
30. Nygård, K.; Hämäläinen, K.; Manninen, S.; Jalas, P.; Ruottinen, J.-P. Quantitative thickness determination using x-ray fluorescence: Application to multiple layers. *X-ray Spectrom.* **2004**, *33*, 354–359. [CrossRef]
31. De Boer, D.K.G. Calculation of x-ray fluorescence intensities from bulk and multilayer samples. *X-ray Spectrom.* **1990**, *19*, 145–154. [CrossRef]
32. De Boer, D.K.G.; Borstrok, J.J.M.; Leenaers, A.J.G.; Van Sprang, H.A. How accurate is the fundamental parameter approach? XRF analysis of bulk and multilayer samples. *X-ray Spectrom.* **1993**, *22*, 33–38. [CrossRef]
33. Gherase, M.R.; Fleming, D.E.B. Calculation of depth-dependent elemental concentration with X-ray fluorescence using a layered calibration method. *Nucl. Instrum. Methods Phys. Res. B* **2011**, *269*, 1150–1156. [CrossRef]

34. Todd, A.C.; Chettle, D.R.; Scott, M.C.; Somervaille, L.J. Monte Carlo modelling of in vivo x-ray fluorescence of lead in the kidney. *Phys. Med. Biol.* **1991**, *36*, 439–448. [CrossRef]
35. Tartari, A.; Fernandez, J.E.; Casnati, E.; Baraldi, C.; Felsteiner, J. EDXRS modelling for in vivo trace element analysis by using the SHAPE code. *X-ray Spectrom.* **1993**, *22*, 323–327. [CrossRef]
36. Vincze, L.; Janssen, K.; Adams, F.; Rivers, M.L.; Jones, K.W. A general Monte Carlo simulation of energy dispersive X-ray fluorescence spectrometers—I: Unpolarized radiation, homogeneous samples. *Spectrochim. Acta* **1993**, *48*, 553–573. [CrossRef]
37. Wallace, J.D. The Monte Carlo modelling of in vivo x-ray fluorescence measurement of lead in tissue. *Phys. Med. Biol.* **1994**, *39*, 1745–1756. [CrossRef]
38. Vincze, L.; Janssen, K.; Adams, F. A general Monte Carlo simulation of energy dispersive X-ray fluorescence spectrometers. II: Polarized monochromatic radiation, homogeneous samples. *Spectrochim. Acta B* **1995**, *50*, 127–147. [CrossRef]
39. Vincze, L.; Janssen, K.; Adams, F. A general Monte Carlo simulation of energy dispersive X-ray fluorescence spectrometers. Part 3. Polarized polychromatic radiation, homogeneous samples. *Spectrochim. Acta B* **1995**, *50*, 1481–1500. [CrossRef]
40. Ao, Q.; Lee, S.H.; Gardner, R.P. Development of the specific purpose Monte Carlo CEARXRF for the design and use of in vivo x-ray fluorescence analysis systems for lead in bone. *Appl. Radiat. Isot.* **1997**, *48*, 1403–1412. [CrossRef]
41. O'Meara, J.M.; Chettle, D.R.; McNeill, F.E.; Prestwich, W.V.; Svensson, C.E. Monte Carlo simulation of source-excited in vivo x-ray fluorescence measurements of heavy metals. *Phys. Med. Biol.* **1998**, *43*, 1413–1428. [CrossRef] [PubMed]
42. Vincze, L.; Janssen, K.; Vekemans, B.; Adams, F. Monte Carlo simulation of X-ray fluorescence spectra. Part 4. Photon scattering at high X-ray energies. *Spectrochim. Acta B* **1999**, *54*, 1711–1722. [CrossRef]
43. Guo, W.; Gardner, R.P.; Todd, A.C. Using the Monte Carlo—Library least-Squares (MCLLS) approach for the in vivo XRF measurement of lead in bone. *Nucl. Instrum. Meth. Phys. Res. A* **2004**, *516*, 586–593. [CrossRef]
44. Zamburlini, M.; Byun, S.H.; Pejović-Milić, B.A.; Prestwich, W.V.; Chettle, D.R. Evaluation of MCNP5 and EGS4 for the simulation of in vivo strontium XRF measurements. *X-ray Spectrom.* **2007**, *36*, 76–81. [CrossRef]
45. Hodoroaba, V.D.; Radtke, M.; Vincze, L.; Rackwitz, V.; Reuter, D. X-ray scattering in X-ray fluorescence spectra with X-ray tube excitation—Modelling, experiment, and Monte-Carlo simulation. *Nucl. Instrum. Meth. Phys. Res. B* **2010**, *268*, 3568–3575. [CrossRef]
46. Schoonjans, T.; Solé, V.A.; Vincze, L.; del Rio, M.S.; Brondeel, P.; Silversmit, G.; Appel, K.; Ferrero, C. A general Monte Carlo simulation of energy-dispersive X-ray fluorescence spectrometers—Part 5. Polarized radiation, stratified samples, cascade effects, M-lines. *Spectrochim. Acta B* **2012**, *70*, 10–23. [CrossRef]
47. Schoonjans, T.; Solé, V.A.; Vincze, L.; del Rio, M.S.; Appel, K.; Ferrero, C. A general Monte Carlo simulation of energy-dispersive X-ray fluorescence spectrometers—Part 6. Quantification through iterative simulations. *Spectrochim. Acta B* **2013**, *82*, 36–41. [CrossRef]
48. Scot, V.; Fernandez, J.E. The Monte Carlo code MCSHAPE: Main features and recent developments. *Spectrochim. Acta B* **2015**, *108*, 53–60. [CrossRef]
49. Sharma, U.; Van Delinder, K.; Gräfe, J.L.; Fleming, D.E.B. Investigating methods of normalization for X-ray fluorescence measurements of zinc in nail clippings using the TOPAS Monte Carlo code. *Appl. Radiat. Isot.* **2022**, *182*, 110151. [CrossRef]
50. Fernández, J.E. XRF intensity in the frame of the transport theory. *X-ray Spectrom.* **1989**, *18*, 271–279. [CrossRef]
51. Fernández, J.E. Polarization effects in multiple scattering photon calculations using the Boltzmann vector equation. *Radiat. Phys. Chem.* **1999**, *56*, 27–59. [CrossRef]
52. Fernández, J.E. Analysis of the effects of geometry on the fluorescence radiation field in the frame of transport theory. *X-ray Spectrom.* **2005**, *34*, 7–10. [CrossRef]
53. Fernández, J.E. Multiple scattering of photons using the Boltzmann transport equation. *Nucl. Instrum. Meth. Phys. Res. B* **2007**, *263*, 7–21. [CrossRef]
54. Fernández, J.E.; Teodori, F. Major and minor contributions to X-ray characteristic lines in the framework of the Boltzmann transport equation. *Quantum Beam Sci.* **2022**, *6*, 20. [CrossRef]
55. Andreo, P. Monte Carlo techniques in medical radiation physics. *Phys. Med. Biol.* **1991**, *36*, 861–920. [CrossRef]
56. Rogers, D.W.O. Fifty years of Monte Carlo simulations for medical physics. *Phys. Med. Biol.* **2006**, *51*, R287–R301. [CrossRef] [PubMed]
57. Rogers, D.W.O. Reflections on a life with Monte Carlo in Medical Physics. *Med. Phys.* **2023**, *50*, 91–94. [CrossRef] [PubMed]
58. Gherase, M.R.; Al-Hamdani, S. A microbeam grazing-incidence approach to L-shell x-ray fluorescence measurements of lead concentration in bone and soft tissue phantoms. *Physiol. Meas.* **2018**, *39*, 035007. [CrossRef] [PubMed]
59. Gherase, M.R.; Al-Hamdani, S. Improvements and reproducibility of an optimal grazing-incidence position method to L-shell x-ray fluorescence measurements of lead in bone and soft tissue phantoms. *Biomed. Phys. Eng. Express* **2018**, *4*, 065024. [CrossRef] [PubMed]
60. Gherase, M.R.; Blaz, S.; Kroeker, S. A novel calibration for L-shell x-ray fluorescence measurements of bone lead concentration using the strontium Kβ/Kα ratio. *Physiol. Meas.* **2021**, *42*, 045011. [CrossRef]
61. Gherase, M.R.; Vargas, A.F. Effective X-ray beam size measurements of an X-ray tube and polycapillary X-ray lens system using a scanning X-ray fluorescence method. *Nucl. Instrum. Meth. Phys. Res. B* **2017**, *395*, 5–12. [CrossRef]
62. Mairs, S.; Swift, B.; Rutty, G.N. Detergent. An alternative approach to traditional bone cleaning methods for forensic practice. *Am. J. Forensic Med. Pathol.* **2004**, *25*, 276–284. [CrossRef] [PubMed]

63. Berger, M.J.; Hubbell, J.H.; Seltzer, S.M.; Chang, J.; Sukumar, R.; Zucker, D.S.; Olsen, K. *XCOM: Photon Cross Section Database, Version 1.5*; National Institute of Standards and Technology: Gaithersburg, MD, USA, 2010.
64. Elam, W.T.; Ravel, B.D.; Sieber, J.R. A new atomic database for X-ray spectroscopic calculations. *Radiat. Phys. Chem.* **2002**, *63*, 121–128. [CrossRef]
65. Press, W.H.; Teukolsky, S.A.; Vetterling, W.T.; Flannery, B.P. *Numerical Recipes*, 3rd ed.; Cambridge University Press: New York, NY, USA, 2007; pp. 120–124.
66. Kroeker, S.E. Energy Spectrum and Exposure Measurements of an X-ray Tube and PXL Produced Microbeam Used in Bone Lead XRF Studies. Master's Thesis, California State University, Fresno, CA, USA, 2021.
67. Bhat, M.; Pattison, J.; Bibbo, G.; Caon, M. Diagnostic x-ray spectra: A comparison of spectra generated by different computational methods with a measured spectrum. *Med. Phys.* **1998**, *25*, 114–120. [CrossRef] [PubMed]
68. Poludniowski, G.; Landry, G.; DeBlois, F.; Evans, P.M.; Verhaegen, F. *SpekCalc*: A program to calculate spectra from tungsten anode x-ray tubes. *Phys. Med. Biol.* **2009**, *54*, N433–N438. [CrossRef] [PubMed]
69. MacDonald, C.A.; Gibson, W.M. Applications and advances in polycapillary optics. *X-ray Spectrom.* **2003**, *32*, 258–268. [CrossRef]
70. ICRU. *Tissue Substitutes in Radiation Dosimetry and Measurement*; Report 44; International Commission on Radiation Units and Measurements: Bethesda, MD, USA, 1989; p. 22.
71. Zhou, H.; Keall, P.J.; Graves, E.E. A bone composition model for Monte Carlo x-ray transport simulations. *Med. Phys.* **2009**, *36*, 1008–1018. [CrossRef]
72. Taylor, J.R. An introduction to error analysis. In *The Study of Uncertainties in Physical Measurements*, 2nd ed.; University Science Books: Sausalito, CA, USA, 1997; pp. 73–77.
73. Ertuğral, B.; Apaydin, G.; Çevik, U.; Ertuğrul, M.; Kobya, A.I. Kβ/Kα X-ray intensity ratios for elements in the range $16 \leq Z \leq 92$ excited by 5.9, 59.5 and 123.6 keV photons. *Radiat. Phys. Chem.* **2007**, *76*, 15–22. [CrossRef]
74. Pejović-Milić, A.; Stronach, I.M.; Gyorffy, J.; Webber, C.E.; Chettle, D.R. Quantification of bone strontium level in humans by in vivo x-ray fluorescence. *Med. Phys.* **2004**, *31*, 528–538. [CrossRef]
75. Zamburlini, M.; Campbell, J.L.; de Silveira, G.; Butler, R.; Pejović-Milić, A.; Chettle, D.R. Strontium depth distribution in human bone measured by micro-PIXE. *X-ray Spectrom.* **2009**, *38*, 271–277. [CrossRef]
76. Möhring, S.; Cieplik, F.; Hiller, K.-A.; Ebensberger, H.; Ferstl, G.; Hermens, J.; Zaparty, M.; Witzgall, R.; Mansfeld, U.; Buchalla, W.; et al. Elemental compositions of enamel or dentin in human and bovine teeth differ from murine teeth. *Materials* **2023**, *16*, 1514. [CrossRef] [PubMed]